Processing and Application of Ceramics 15 [1] (2021) 58–68
https://doi.org/10.2298/PAC2101058S

Effect of calcination atmosphere on structural, optical and photocatalytic activity of TiO_2/SnS_2 core-shell nanostructures in the reduction of aqueous Cr(VI) to Cr(III)

Shalini Sikdar[1,2], Tiju Thomas[3], M.S. Ramachandra Rao[2], Subramshu S. Bhattacharya[1,*]

[1]*Nano Functional Materials Technology Centre (NFMTC), Department of Metallurgical and Materials Engineering, Indian Institute of Technology Madras, Chennai – 600 036, India*
[2]*Nano Functional Materials Technology Centre (NFMTC), Material Science and Research Centre, Department of Physics, Indian Institute of Technology Madras, Chennai – 600 036, India*
[3]*Applied Nanostructures Engineering and Nanochemistry Lab, Department of Metallurgical and Materials Engineering, Indian Institute of Technology Madras, Chennai – 600 036, India*

Received 29 September 2020; Received in revised form 11 January 2021; Accepted 1 February 2021

Abstract

Conversion of Cr(VI) to Cr(III) in mitigating pollution of water bodies is of significant importance to public health due to the fact that Cr(VI) is known to be a potent carcinogen, while Cr(III) is relatively low in toxicity. Photocatalytic approaches are considered as important means to achieve this reduction. Here, TiO_2/SnS_2 core-shell nanostructures have been produced using a single-step hydrothermal method and its photocatalytic activity is tested for the reduction of aqueous Cr(VI). The structural and optical properties of the as-synthesized products are characterized by XRD, HRTEM, Raman, FTIR, XPS and DRS techniques. The present work reveals that by calcining the core-shell nanoparticles in Ar atmosphere a defective Ti_3O_5 phase is formed as the core with low band gap, and hence, offers improved light absorption in the visible range. However, its photoactivity was found to be lower than that of the core-shell nanoparticles annealed in oxidizing atmosphere. The observed lower photoreduction was due to the presence of midgap states which acted as recombination centres and hence, reduced the photocatalytic activity.

Keywords: *hydrothermal synthesis, TiO_2/SnS_2 core-shell nanoparticles, photocatalyst, defective Ti_3O_5 nanorods*

I. Introduction

Cr(VI) is a common contaminant found in effluent waste waters from industries that carry out leather processing, paint manufacturing, chromate salt production etc. [1]. Due to its high level of toxicity, the maximum concentration of Cr(VI) in drinking water and in industrial wastewaters/effluents are regulated globally. The easiest method to treat Cr(VI) is to convert it to the less toxic Cr(III) which can then be precipitated as $Cr(OH)_3$ [2]. However, the conventional chemical reduction methods need significant use of a reducing agent such as ferrous sulphate, which is not scalable and also imposes significant cost. On the other hand, semiconductor mediated photocatalytic reduction of Cr(VI) has advantages such as simple operation, cost effectiveness, high efficiency, dependence on natural solar energy and no discharge of unwanted soluble chemicals [3,4]. To this end, several researchers have reported on the photocatalytic activity of semiconductors like TiO_2, SnO_2, ZnO, CeO_2 and $SrTiO_3$ [5–7]. However, in all these cases, the photoreduction yield leaves much scope for improvement. Towards the improvement of photoreduction catalysts useful for the reduction of Cr(VI), use of core-shell nano heterostructures appear to be a promising direction. Recent developments show that core-shell nano heterostructures deployed for photovoltaic and photocatalysis applications indicate substantial potential for practical use [8]. Type II core-shell structures [9–11] have an alignment of va-

* Corresponding author: tel: +91 44 22574765,
e-mail: *ssb@iitm.ac.in*

lence and conduction bands such that one charge carrier is confined to the core while the other is confined to the shell. In addition, a combination of phases used in the core and shell allow absorption of wavelengths that would otherwise not be possible with a single material.

In this investigation, we choose TiO_2 as the core material. TiO_2 is already a well-known semiconductor material for photocatalysis applications [12]. TiO_2 based nanostructures have been shown to be promising due to their excellent stability, lesser electron-hole recombination and efficient transport properties [13]. However, due to its wide band gap (3.0–3.3 eV), the efficiency in the solar spectrum is relatively poor. Hence, TiO_2 works well only when coupled with lower band gap semiconductors as sensitizers [14]. Unfortunately, these semiconductor sensitizers are toxic and very often unstable [15]. This imposes a practical set of problems too. Hence, it is necessary to find nontoxic semiconductor materials as sensitizers, which could be used as a shell with a TiO_2 core. Within these constraints, sulphide nanomaterials like SnS_2 which have low band gap (E_g = 2.3 eV) and lower toxicity [16] appear to show a lot of potential. It may in fact be noted that SnS_2/TiO_2 nanocomposites display excellent photocatalytic degradation of aqueous Cr(VI) due to the formation of a heterojunction [17]. However, till date TiO_2/SnS_2 core-shell nanoparticles with TiO_2 core and SnS_2 shell have not been reported.

Recently, the presence of an intrinsic defect in the TiO_2 matrix, like oxygen vacancy ($V_O^{\bullet\bullet}$) has been shown to trigger visible light activity of TiO_2 [18]. Previous reports showed that annealing of TiO_2 nanoparticles in hydrogen can produce defective "black" titania nanoparticles with a stoichiometry of Ti_nO_{2n-1} and a narrow band gap of ~1.0 eV [19]. Under this situation, black TiO_2 can aid in improved light absorption in the visible regime, and hence appear to offer considerably improved prospects for photocatalytic activity over "white" TiO_2. Generally, visible light photocatalytic activity of semiconductors depends on factors such as: efficient full solar spectrum absorbance, electronic band structure, photoactive surfaces and interfaces, charge separation and charge recombination [20]. The electronic band structure, especially the sub-band gap states, plays a very important role in governing these factors. For the sub-band gap states to be photocatalytically active, they must have a favourable energetic location for the desired reaction and should offer adequate lifetimes for the excited charge carriers to participate in the photochemical reaction [21]. These complex interplays of sub-band gap states essentially mean that one-on-one correlation between increased light absorption and increased photoactivity would not necessarily be true.

The aim of the present work was to synthesise TiO_2/SnS_2 core-shell nanostructures in a single-step hydrothermal route followed by calcination in oxidizing or Ar atmospheres to induce the formation of pure rutile TiO_2 or with defective Ti_3O_5 phase in the core. The structural and optical properties of the TiO_2/SnS_2 nanoparticles were investigated and their influence on the photocatalytic activity in the reduction of Cr(VI) to Cr(III) was explored.

II. Experimental details

2.1. Materials

All chemicals were of analytical grade and were used without further purification. Tin(IV) chloride pentahydrate ($SnCl_4 \cdot 5\,H_2O$, 99% purity), thioacetamide (C_2H_5NS, 99% purity), titanium tetra iso-propoxide (TTIP, 99% purity) and acetic acid (99% purity) were purchased from Alfa Aesar, India. Ethanol (99.9%, A.R.) was obtained from Merck, India.

2.2. Preparation of samples

A simple hydrothermal method was used to produce the core-shell nanostructures. 0.5 ml of titanium tetra iso-propoxide (TTIP) was stirred with 1 ml ethanol. Thereafter, an SnS_2 precursor consisting of 0.01 mol $SnCl_4 \cdot 5\,H_2O$ and 0.02 mol C_2H_5NS and 40 ml of 5 vol.% acetic acid aqueous solution was added in a dropwise manner. The mixture was stirred continuously and vigorously for 15–20 min until a clear homogeneous solution was obtained. This solution was then transferred to Teflon-lined stainless-steel autoclaves of capacity 50 ml and the sealed autoclaves were maintained at 180 °C for 12 h. This was followed by natural cooling to room temperature. The as-formed yellow precipitates of TiO_2/SnS_2 core-shell nanoparticles were filtered and washed with distilled water and ethanol and finally dried in a hot air oven at 80 °C for 1–2 h. Thereafter, the powders were calcined in an oxidising atmosphere at 300 °C for 1 h (labelled as CS1). Another batch (also hydrothermally synthesized at 180 °C for 12 h) was calcined in Ar atmosphere at 300 °C for 1 h (labelled as CS2).

SnS_2 and TiO_2 were also synthesized separately via hydrothermal reactions of their respective precursors (0.01 mol $SnCl_4 \cdot 5\,H_2O$ + 0.02 mol C_2H_5NS + 40 ml 5 vol.% acetic acid aqueous solution for SnS_2) and (0.5 ml TTIP + 1 ml ethanol + 40 ml 5 vol.% acetic acid aqueous solution for TiO_2) at 180 °C for 12 h. The as-produced TiO_2 nanoparticles were calcined at 300 °C for 1 h in both oxidizing (labelled as TiO_2-O) and Ar atmosphere (labelled as TiO_2-Ar).

2.3. Characterization

Phase identification of the core-shell nanomaterials was carried out by X-ray diffraction (Pan Analytical Xpert Pro) in the 2θ range from 10° to 90° with Cu K_α radiation using a step size of 0.02°. The microstructures were investigated by HRTEM (Technai G Twin F-20). Raman spectra were obtained at room temperature with a Witec alpha 300R Raman spectrometer using 532 nm excitation wavelength and the chemical states of the elements were measured by XPS (SPECS HSA-3500). The vibration modes of the as-synthesized samples were

studied using FTIR spectroscopy (Perkin Elmer system one FTIR) and UV-Vis absorption spectroscopy using a Hitachi U3300 spectrophotometer was used to determine the optical and photocatalytic parameters of the samples.

2.4. Photocatalytic tests

Photocatalytic properties of the as-synthesized products were tested using the reduction of aqueous $K_2Cr_2O_7$ solution under visible light ($\lambda > 420$ nm) irradiation. This was carried out in a photochemical reactor using a 300 W Xenon lamp. A water-cooled jacketed quartz tube was used to separate the light source from reaction mixture which ensured minimal transfer of heat from the lamp to the reaction chamber. This was essential so as to avoid thermal degradation (thermolysis) of the $K_2Cr_2O_7$ solution. Before illumination, 100 ml of 160 mg/l $K_2Cr_2O_7$ (Alfa Aesar, 99%) solution containing 50 mg of photocatalyst was magnetically stirred in the absence of light for 2 h. For all the photocatalytic reactions, the $K_2Cr_2O_7$ solution was kept at a chosen distance from the light source. For studying the progress of the degradation reactions, 4 ml of the solution was taken from the reactor during illumination at scheduled intervals and centrifuged to separate the photocatalyst. Following this step, UV-Vis spectroscopic measurements were made in order to determine the concentration of the $K_2Cr_2O_7$ solution. In order to quantify the photocatalytic activities of TiO_2, SnS_2 and the core-shell nanoparticles, the following definition was used for photo-degradation efficiencies (PDE_t):

$$PDE_t = \frac{C_0 - C_t}{C_0} \times 100 \quad (1)$$

Here, C_0 and C_t are concentrations of the $K_2Cr_2O_7$ solution at irradiation time of 0 (soon after dark adsorption equilibrium is achieved and at the outset of the irradiation experiment) and after t minutes, respectively.

III. Results and discussion

3.1. XRD analysis

XRD patterns of the as-synthesized core-shell nanoparticles as well as the pure TiO_2 and SnS_2 nanoparticles calcined under different atmospheres are shown in Fig. 1. The diffraction peaks were indexed to hexagonal berndite SnS_2 (JCPDS no. 98-004-8478) and tetragonal rutile TiO_2 (JCPDS no. 98-004-6116) respectively (Fig. 1a). The tetragonal anatase phase (JCPDS no-98-010-933) can be detected in both TiO_2-O and TiO_2-Ar (Fig. 1c). A shift of the diffraction peaks corresponding to TiO_2 toward lower angles was observed for the TiO_2-Ar (Fig. 1d) as well as for the CS2 sample (Fig. 1b), due to the formation of oxygen deficient Ti_nO_{2n-1}. While no diffraction peaks corresponding to Ti_3O_5 were evident in the XRD patterns, the possibility of Ti_3O_5 forming could not be ruled out as the quantity could be less than

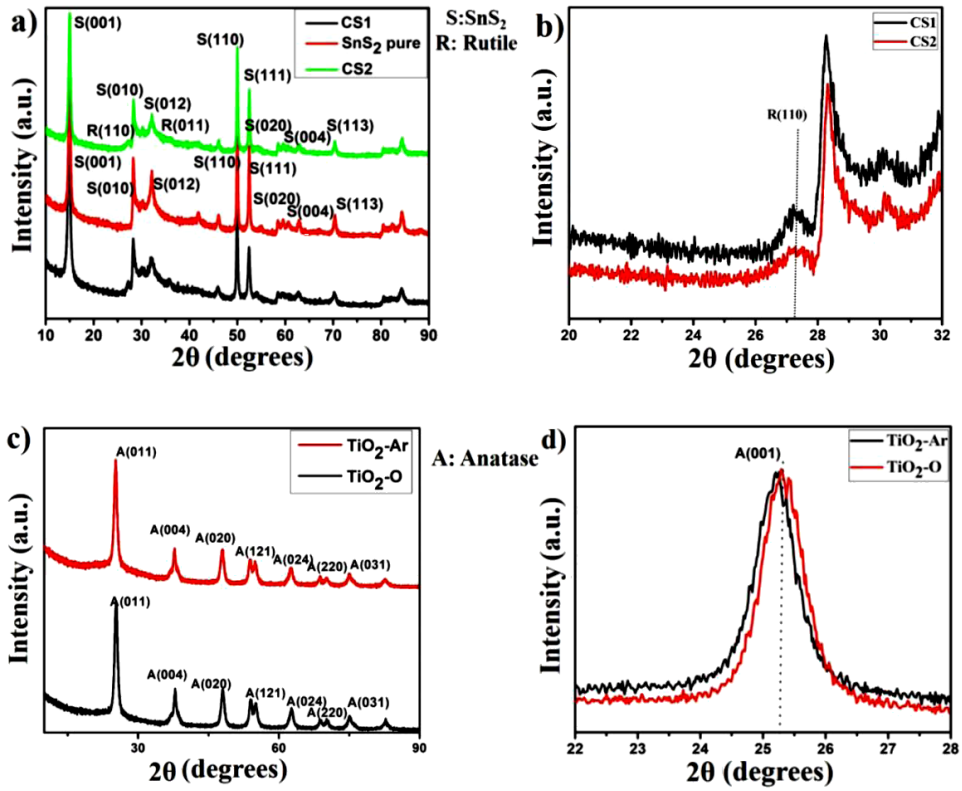

Figure 1. XRD pattern of core-shell nanoparticles - CS1, CS2 and pure SnS_2 (a), XRD pattern (magnified) corresponding to TiO_2 peak (110) of CS1 and CS2 (b), XRD pattern of TiO_2-O and TiO_2-Ar (c) and XRD pattern (magnified) corresponding to TiO_2 peak (001) of TiO_2-O and TiO_2-Ar (d)

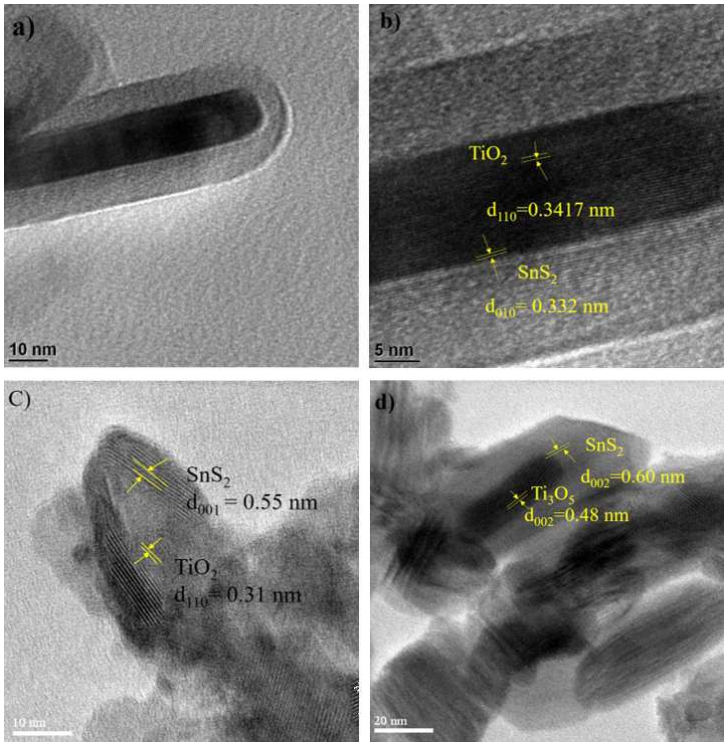

Figure 2. HRTEM images of core-shell nanoparticles: a) CS1, b) magnified view of CS1, c) CS2 with rutile TiO_2 nanorods and d) CS2 with Ti_3O_5 nanorods

the detection threshold limit of XRD. Thus, in order to detect and quantify the existence of Ti_3O_5, HRTEM and XPS experimental results were investigated.

3.2. Microstructural study

HRTEM was used to reveal the structure and study the detailed morphology of the as-synthesized samples (Fig. 2). In case of the sample CS1 (Fig. 2b), core-shell nanoparticles consisting of rutile TiO_2 nanorods of 71 nm length and 12 nm diameter coated with SnS_2 with a shell thickness of 10 nm were seen. The lattice fringe spacing of the core was 0.34 nm matching with the {110} planes of rutile TiO_2 while that of the shell was 0.33 nm matching with the {010} planes of SnS_2.

In case of the sample CS2, rutile TiO_2 nanorods (30 nm length, 10 nm diameter) (Fig. 2c) as well as defective Ti_3O_5 nanorods (41 nm length, 10 nm diameter) (Fig. 2d) coated with SnS_2 having a shell thickness of 5 nm and 18 nm, respectively, were seen. The lattice fringe spacing of the core for rutile TiO_2 was 0.31 nm matching with the {110} planes, while the lattice fringe spacing of the defective Ti_3O_5 core was 0.48 nm matching with the {002} planes of Ti_3O_5 and the lattice fringes spacings of the shell in both cases were 0.60 nm matching with the {002} planes of SnS_2. It is believed that oxygen vacancies ($V_O^{\bullet\bullet}$) created in the rutile TiO_2 structure during the annealing in Ar atmosphere induced lattice stresses resulting in the formation of the distorted oxygen-deficient Ti_3O_5 phase with an expansion in the lattice spacing. These results demonstrate that calcination atmosphere is a critical parameter for phase control of TiO_2 based core-shell nanostructures.

3.3. Raman spectroscopy analysis

Raman spectroscopy, performed using an excitation wavelength 532 nm revealed the defects induced as well as other changes in the local structure of the core-shell nanoparticles (Fig. 3a). The Raman spectrum of the SnS_2 reveals a peak at 302 cm^{-1} (A_{1g} mode of SnS_2) [16] while the pure TiO_2-O and TiO_2-Ar (Fig. 3b) both show the B_{1g} mode (400 cm^{-1} and 515 cm^{-1}) and B_{2g} mode (637 cm^{-1}) of anatase [22] with an additional large and broad peak at 2600 cm^{-1} in case of the TiO_2-Ar indicating the presence of oxygen vacancies [23]. For all the core-shell nanostructures, blue shift of the Raman band occurred for SnS_2 (302 cm^{-1} to 311 cm^{-1}) as well as a red shift of rutile TiO_2. The shift in the Raman band of SnS_2 was due to the tensile strain in the shell induced by the core [24]. Red shift of about 20 cm^{-1} in the Raman band of rutile TiO_2 (612 cm^{-1} to 592 cm^{-1}) in case of the CS2 compared to CS1 indicated that the original TiO_2 lattice had broken down into a disordered Ti_3O_5 phase with some amount of oxygen vacancies [18] which was further confirmed by XPS results.

3.4. FTIR analysis

FTIR spectroscopy (Fig. 4) was also performed to investigate the vibrational modes of the core-shell nanoparticles (CS1 and CS2) as well as the TiO_2 nanoparticles (TiO_2-O and TiO_2-Ar). For the pure SnS_2, the peaks at 633 cm^{-1} and 1115 cm^{-1} were found to be related with vibrations of the Sn–S bonds [25]. The band at 1623 cm^{-1} may be attributed to the bending mode of OH bonds [26]. The broad band appearing at 3400 cm^{-1}

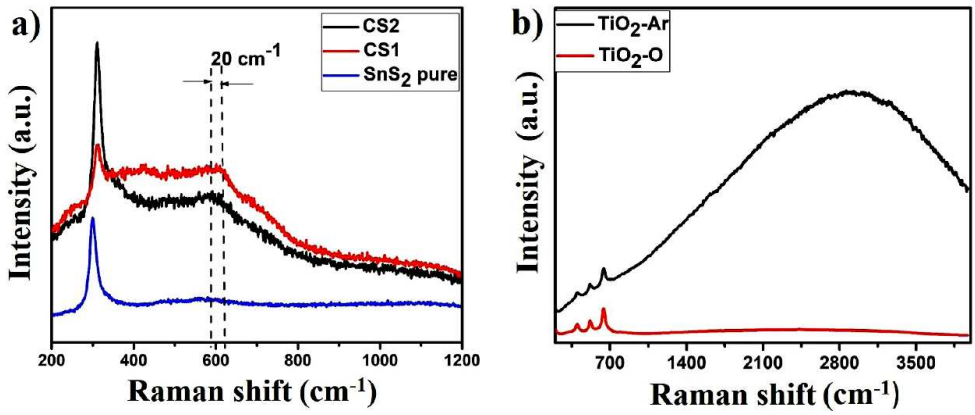

Figure 3. Raman spectra of: a) core-shell nanoparticles and b) TiO_2-O and TiO_2-Ar

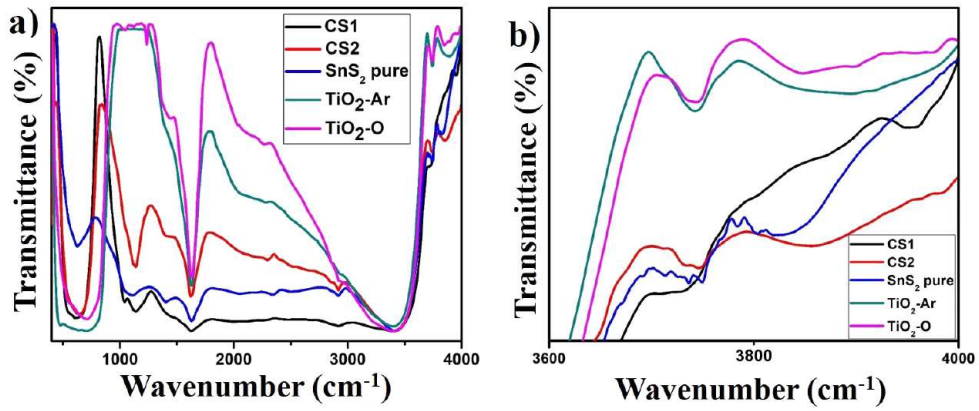

Figure 4. FTIR spectra of: a) core-shell nanoparticles CS1, CS2, SnS_2 and TiO_2 and b) FTIR spectra of the -OH stretching region measured for TiO_2, SnS_2 and core-shell nanoparticles

as well as the peak at 3742 cm^{-1} present in the TiO_2, SnS_2 and the core-shell nanomaterials were attributed to surface hydroxyl groups [26]. For the hydrothermally synthesized TiO_2-O and TiO_2-Ar, the peaks at 400–800 cm^{-1} were ascribed to the bending modes of Ti–O bonds [27]. The spectra showed features of complex vibrations due to TiO_2 and Ti_2O_3. The band at 3848 cm^{-1} for the TiO_2-O was due to the presence of tetrahedrally coordinated vacancies designated as ${}_4Ti^{4+}-OH$, whereas the band at 3897 cm^{-1} was due to octahedral vacancies designated as ${}_6Ti^{3+}-OH$ arising from the result of water adsorption of the Ti^{3+} states of Ti_3O_5 [28]. Formation of the core-shell nanostructures resulted in a shift in the band positions corresponding to the Sn–S bands of SnS_2 as well as Ti–O bands of the samples TiO_2-O and TiO_2-Ar [29].

3.5. XPS analysis

XPS was used to investigate the essential components and oxidation states of the as-synthesized SnS_2, TiO_2 and TiO_2/SnS_2 core-shell nanostructures as well as to understand the nature of the Ti_3O_5 chemical bonds. Figures 5 and 6 show the XPS spectra of the CS1 and CS2 confirming the presence of Ti, O, Sn and S. The spectra of both CS1 and CS2 showed peaks located at 459 eV and 465 eV which corresponded to Ti $2p_{3/2}$ and Ti $2p_{1/2}$, respectively, confirming the existence of Ti^{4+} in both CS1 and CS2 with additional peaks at 457 eV which corresponded to the Ti^{3+} state of Ti_2O_3 in case of the CS2 [28]. On the other hand, O 1*s* of CS1 consisted of two peaks – 532.1 eV ($Ti^{4+}-O$) and 534.6 eV (OH^-) [30]. Likewise for CS2 O 1*s*, the peaks could be deconvoluted into three peaks – 530.5 eV ($Ti^{4+}-O$), 532.1 eV ($Ti^{3+}-O$) and 533.5 eV (OH^-) [30,31]. For the CS2, the binding energies of Sn $3d_{5/2}$ (487 eV), Sn $3d_{3/2}$ (496 eV) and S $2p_{1/2}$ (163 eV), and for the CS1, binding energies corresponding to Sn $3d_{5/2}$ (486.5 eV), Sn $3d_{3/2}$ (495 eV), S $2p_{3/2}$ (161.5 eV) and S $2p_{1/2}$ (162.7 eV) were observed. It was seen that the binding energy of O 1*s* showed a positive shift of about 1.4 eV from 530.6 eV to 532 eV for CS1 and a negative shift of about −0.6 eV from 530.6 eV to 530 eV for the CS2 in comparison with O 1*s* of the TiO_2-O and TiO_2-Ar samples. This may be due to the close contact between the TiO_2 and SnS_2 nanoparticles, which formed a heterojunction with some electrons being transferred from the SnS_2 shell to the TiO_2 core [32]. Minor shifts in the binding energies values of Sn $3d_{5/2}$, Sn $5d_{1/2}$ as well as S $2p_{1/2}$ of CS2 and CS1 were also observed compared to the corresponding values in case of bulk SnS_2 [33].

The formation of the Ti_3O_5 chemical bonds can be explained from the XPS spectrum of the sample TiO_2-

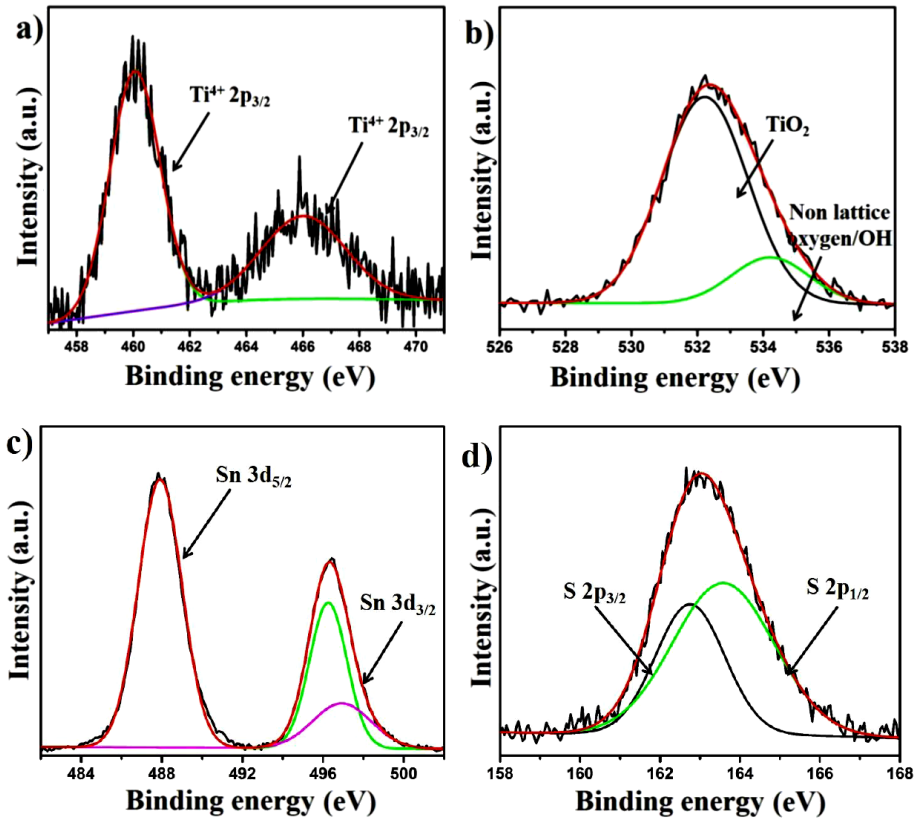

Figure 5. XPS spectra of core-shell nanoparticles CS1 with the deconvolution: a) Ti 2*p* core level, b) O 1*s* core level, c) Sn 3*d* core level and d) S 2*p* core level

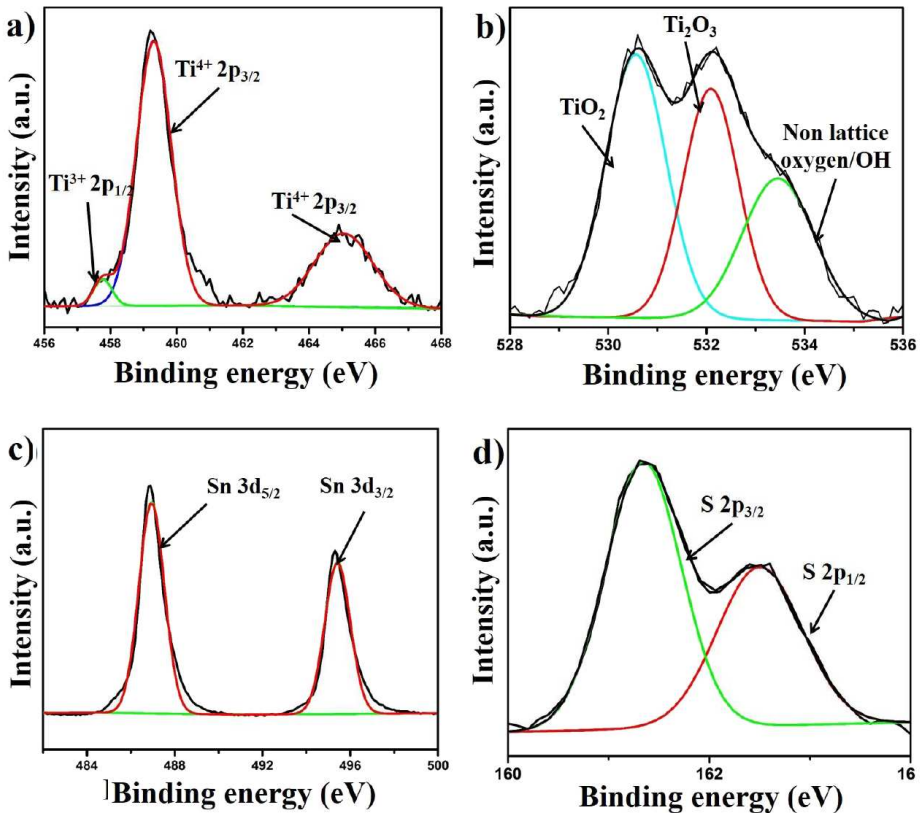

Figure 6. XPS spectra of core-shell nanoparticles CS2 with the deconvolution: a) Ti 2*p* core level, b) O 1*s* core level, c) Sn 3*d* core level and d) S 2*p* core level

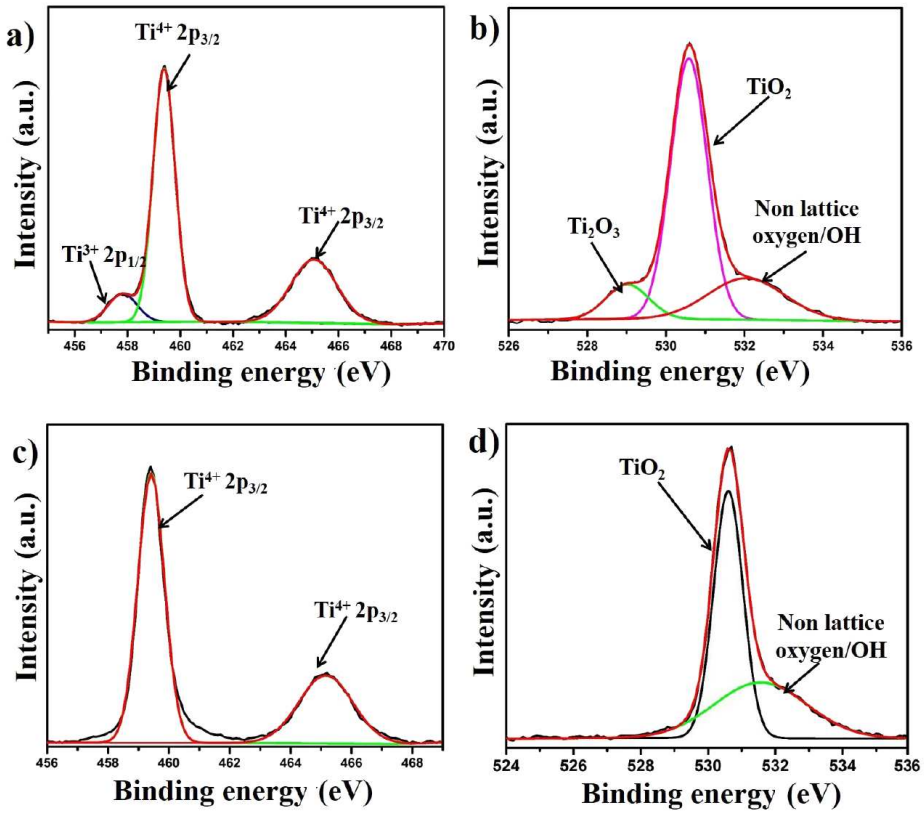

Figure 7. XPS spectra of TiO_2-O and TiO_2-Ar with the deconvolution: a) Ti 2*p* core level, b) O 1*s* core level of TiO_2-Ar, c) Ti 2*p* core level and d) O 1*s* core level of TiO_2-O

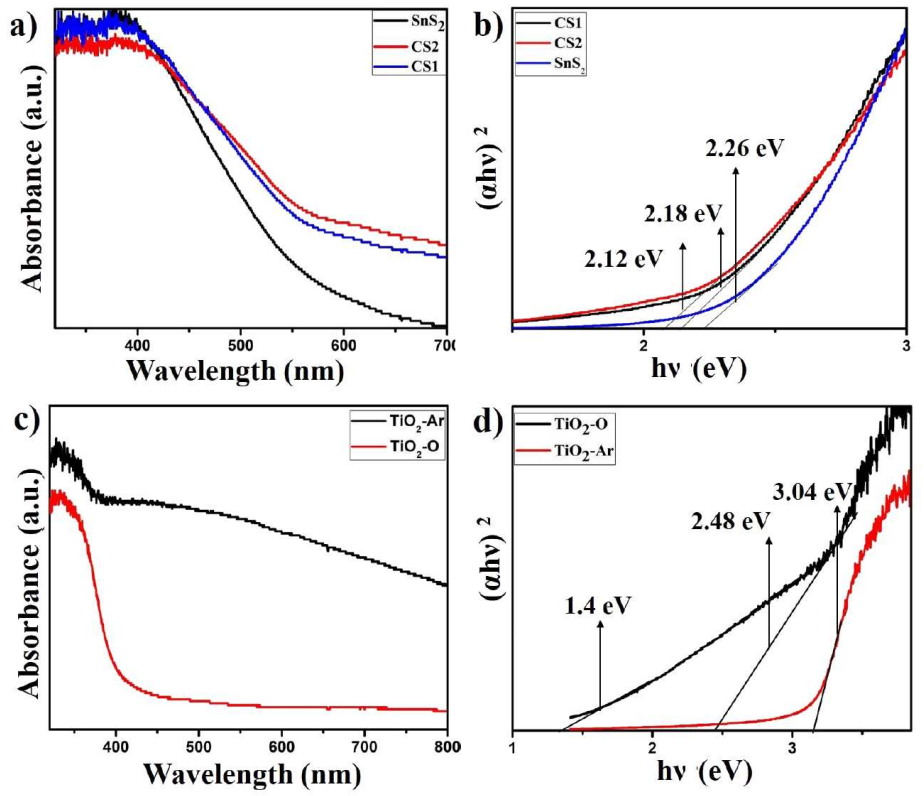

Figure 8. UV-vis DRS of CS1, CS2, SnS_2 and TiO_2 nanoparticles (a, c) and band gap evaluation from the Tauc plots of CS1, CS2, SnS_2 and TiO_2 nanoparticles (b, d)

Ar (Figs. 7a and 7b). The Ti 2*p* spectrum of the TiO_2-Ar (Fig. 7a) was resolved into three components where the binding energy value of 457 eV was identified with the +3 oxidation state of Ti in Ti_2O_3, while those at 459.4 eV and 465 eV were identified with the +4 oxidation state of Ti in TiO_2 [28,30]. The O 1*s* (Fig. 7b) spectrum consisted of three peaks: 528.9 eV (assigned to oxygen bonded to Ti^{3+}), 530.5 eV (Ti^{4+}–O), and 532.3 eV (OH^-) [28]. Quantitatively, 67.3% were due to Ti^{4+} believed to be arising from the reaction of the surface (Ti^{3+}) states of the Ti_3O_5 nanoparticles with water during hydrothermal synthesis. It was seen that the (Ti^{3+}/Ti^{4+}) ratio was (1:10) which was much lower than the expected value for a Ti_3O_5 phase (2:1) [34]. This implied that the amount of Ti_3O_5 formed during hydrothermal synthesis was very low (and, therefore, could not be detected in the XRD pattern). The formation of Ti^{3+} was closely associated with the presence of oxygen vacancies which was calculated to be 11.6% using the ratio of the areas under the Ti^{3+} $2p_{3/2}$ peak and the Ti^{4+} $2p_{3/2}$ peak.

3.6. Optical studies

Diffuse reflectance spectroscopy (DRS) of the samples was carried out to determine the band gap energy and results are presented in Fig. 8. The direct band gaps (E_g) were estimated from the Tauc plots (Figs. 8b and 8d). The band gap of the pure SnS_2 was 2.26 eV and those of the pure TiO_2-O and TiO_2-Ar were 3.04 eV and 2.48 eV, respectively. For the TiO_2-Ar an additional lower band gap of 1.4 eV was also observed which was due to the presence of oxygen vacancies [35]. The band gaps of the CS1 and CS2 nanoparticles were 2.18 eV and 2.12 eV, respectively. The absorption intensity of the core-shell nanoparticles was higher compared to the pure TiO_2-O. In case of the CS2, the decrease in the band gap occurred due to the formation of the defective Ti_3O_5 as core with oxygen vacancies. DRS absorption measurements of the TiO_2-Ar (Fig. 8c) showed a broad absorption over the entire visible spectrum indicating that the oxygen vacancies helped in generating a sub-band just below the conduction band edge of pure TiO_2 thereby narrowing the band gap to 1.4 eV. Hence, it is evident that the calcination atmosphere was a critical parameter in controlling the band gap of the TiO_2/SnS_2 core-shell nanostructures.

3.7. Photocatalytic performance

The photocatalytic activities of the SnS_2, TiO_2, and the TiO_2/SnS_2 core-shell nanoparticles in the reduction of aqueous Cr(VI) under visible light irradiation are shown in Fig. 9a. It can be seen that in the presence of the TiO_2-Ar nanoparticles, very little reduction of Cr(VI) took place under visible light irradiation for 120 min. On the other hand, the reduction took place rapidly in the presence of the CS1 and CS2 as well as the SnS_2 nanoparticles. The photocatalytic activity followed the order: CS1 > SnS_2 > CS2 > TiO_2-O > TiO_2-Ar. The variation of C/C_0 with time indicated that in 60 min the $K_2Cr_2O_7$ in the solution degraded by 21%,

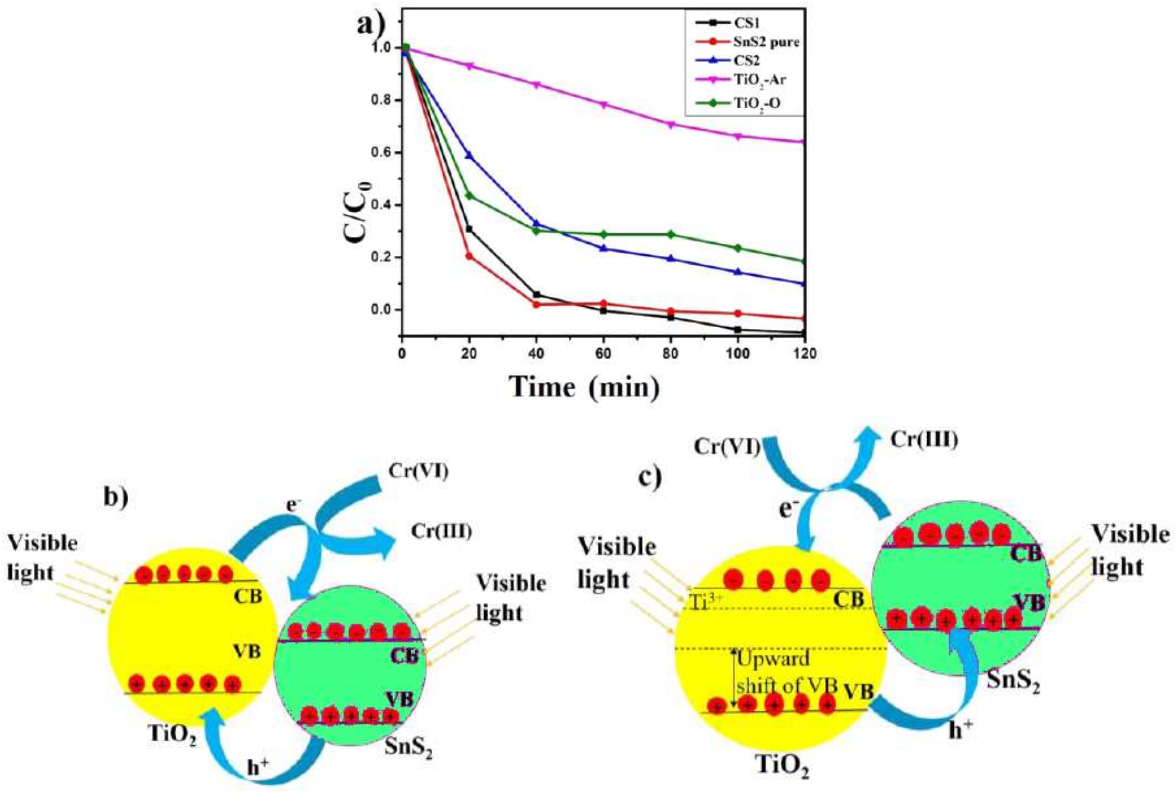

Figure 9. Photocatalytic degradation curves of core-shell nanoparticles CS1 and CS2, SnS_2, TiO_2-O and TiO_2-Ar (a) and schematic diagrams of electronic transition between TiO_2 and SnS_2 under visible light irradiation for CS1 (b) and CS2 (c)

67%, 72%, 100% and 95% in the presence of the TiO_2-Ar, TiO_2-O, CS2, CS1 and SnS_2, respectively. Although the pure SnS_2 nanoparticles showed higher photocatalytic reduction at higher concentrations of Cr(VI), later the core-shell nanomaterial CS1 showed slightly better performance when compared to the pure SnS_2 and TiO_2 nanoparticles as well as the CS2 core-shell nanoparticles.

Mechanism of photocatalytic degradation

The relative band edge positions associated with both CS1 and CS2 revealed the mechanism of photocatalytic activity (shown schematically in Fig. 9b and Fig. 9c, respectively). For the CS1 nanoparticles, the valence band edges of TiO_2 and SnS_2 are −2.87 eV [36] and −1.76 eV [37], respectively, with respect to the vacuum level and the valence band offset was determined by using the following expression [36]:

$$\Delta E_v = (E_v - E_{cl})_{TiO_2} - (E_v - E_{cl})_{SnS_2} + \Delta E_{cl} \quad (2)$$

where $(E_v - E_{cl})$ is the difference between the valence band maximum and a conveniently identifiable core level (which in this case is Ti_{2p} and Sn_{3d} while ΔE_{cl} is the difference between the characteristic core levels in TiO_2 and SnS_2, where the heterojunction had formed). For the CS1 nanoparticles, although a large valence band offset value (−1.36 eV) existed between TiO_2 and SnS_2, this heterojunction could be anticipated as a type II heterojunction. In this system, upon excitation, photogenerated electrons from the higher energy conduction band (CB) of TiO_2 moved towards the conduction band of SnS_2 and holes generated in the valence band (VB) of SnS_2 moved towards the valence band of TiO_2. The electrons in the CB of SnS_2 reacted with the dichromate ions converting Cr(VI) to Cr(III). However, at the same time some of these electrons reacted with the adsorbed oxygen to produce $^{\bullet}O_2^-$ radicals, which, in turn, generated hydroxyl radicals ($^{\bullet}OH$) by reacting with H_2O. These hydroxyl radicals ($^{\bullet}OH$) oxidised some of the Cr(III) back to Cr(VI) to a limited extent [38]. The reactions can be described as follows:

$$TiO_2 + h\nu(\text{visible}) \longrightarrow TiO_2(e^-CB + h^+VB) \quad (3)$$

$$SnS_2 + h\nu(\text{visible}) \longrightarrow SnS_2(e^-CB + h^+VB) \quad (4)$$

$$TiO_2(e^-CB) \longrightarrow SnS_2(e^-CB) \quad (5)$$

$$SnS_2(h^+VB) \longrightarrow TiO_2(h^+VB) \quad (6)$$

$$2\,Cr_2O_7^{2-} + 3\,(e^-CB)_{SnS_2} + 2\,OH^+ \longrightarrow 4\,Cr^{3+} + 10\,H_2O + 2\,O_2 \quad (7)$$

$$SnS_2(e^-CB) + O_2 \text{ dissolved} \longrightarrow {}^{\bullet}O_2^- \quad (8)$$

$$^{\bullet}O_2^- + H_2O \longrightarrow {}^{\bullet}O_2H + OH^- \quad (9)$$

$$^{\bullet}O_2^- + H^+ \longrightarrow {}^{\bullet}O_2H \quad (10)$$

$$^{\bullet}O_2H + OH^- \longrightarrow H_2O_2 + {}^{\bullet}OH \quad (11)$$

$$H_2O_2 \longrightarrow 2\,(^{\bullet}OH) \quad (12)$$

$$3\,(^{\bullet}OH) + Cr^{3+} \longrightarrow Cr^{6+} + 3\,OH^- \quad (13)$$

On the other hand, in case of the CS2 sample upon excitation, photogenerated electrons from the higher energy conduction band (CB) of SnS_2 moved towards the conduction band of TiO_2 while holes generated in the valence band (VB) of TiO_2 moved towards the valence band of SnS_2. While the majority of the electrons in the CB of TiO_2 resulted in the generation of $^{\bullet}O_2^-$ radicals and reduced Cr(VI) to Cr(III), some of the $^{\bullet}O_2^-$ radicals formed hydroxyl radicals ($^{\bullet}OH$) that oxidised Cr(III) back to Cr(VI) to a limited extent, thereby decreasing the rate of photodegradation. In addition to the reactions (3, 4 and 9–13), the following reactions took place:

$$SnS_2(e^-CB) \longrightarrow TiO_2(e^-CB) \quad (14)$$

$$TiO_2(h^+VB) \longrightarrow SnS_2(h^+VB) \quad (15)$$

$$2\,Cr_2O_7^{2-} + 3\,(e^-CB)_{TiO_2} + 2\,OH^+ \longrightarrow 4\,Cr^{3+} + 10\,H_2O + 2\,O_2 \quad (16)$$

$$TiO_2(e^-CB) + O_2 \text{ dissolved} \longrightarrow {}^{\bullet}O_2^- \quad (17)$$

At higher concentrations of Cr(VI), the CS1 nanoparticles showed slightly lower photocatalytic reduction activity than the pure SnS_2 nanoparticles due to the fact that the amount of produced hydroxyl radicals was higher in the case of CS1 leading to the oxidation of Cr(III) back to Cr(VI). However, after 40 min of photocatalytic degradation, the reduction rate for SnS_2 nanoparticles decreased due to the trapped adsorbed O_2 on the SnS_2 surface reducing the available active sites for degradation [39]. On the other hand, in the case of CS1, due to the special core-shell morphology and type II heterojunction formed at the TiO_2/SnS_2 interface, an improved photoreduction compared to SnS_2 nanoparticles was observed at the later stage of photodegradation.

So, when the TiO_2/SnS_2 core-shell nanoparticles were used, an enhancement in the photocatalytic reduction activity could be expected *vis-à-vis* a single-phase material, as the recombination of photogenerated carriers was suppressed in this heterostructured material. The above offers a reasonable explanation as to why the CS1 showed the highest photocatalytic reduction activity when compared to the single phase SnS_2 and TiO_2.

On the other hand, despite having a type II heterojunction at TiO_2/SnS_2 interface, the CS2 showed lower photocatalytic activity than the CS1 as well as SnS_2. From the energy band diagram of the CS2 sample it can be seen that the valence band maximum due to oxygen vacancies moved by 1.79 eV towards the TiO_2 conduction band minimum edge [35] and resulted in the formation of a narrow band gap (E_g = 1.4 eV) of TiO_2. At the same time, the Ti^{3+} defect states in the TiO_2-Ar caused a sub-band formation between the CB and VB of TiO_2 and the resulting midgap state acted as a charge recombination centre, thereby increasing the recombination rate, and, consequently, reduced the photocatalytic activity of CS2 [21] (as seen schematically in Fig. 9c).

IV. Conclusions

TiO_2/SnS_2 core-shell nanostructures were successfully prepared using a single-step hydrothermal method and the photocatalytic activity was tested for the reduction of aqueous Cr(VI). The core-shell nanoparticles were modified by annealing in air (sample: CS1) and Ar atmosphere (sample: CS2). The core of the latter sample was found to be rich in oxygen vacancies and had a lower band gap (~1.4 eV). However, the CS1 sample performed much better at photoreduction than the individual constituent phases (TiO_2 and SnS_2). This was attributed to a type II heterojunction being formed at the TiO_2/SnS_2 interface, which offered effective photoreduction. On the other hand, the improved light absorption characteristics of the CS2 sample due to lowered band gap resulted in poorer photoreduction performance when compared to the CS1 sample. This was due to the presence of midgap states which acted as recombination centres, and hence, reduced the photocatalytic activity in the visible spectrum. Given the above results, the work offers fresh insights into the prospects of sulphide-oxide core-shell nanostructures in producing next-generation photoreduction catalysts.

Acknowledgements: We acknowledge the immense support from Nanotechnology Lab and Laboratory for High Temperature Ceramics, Department of Metallurgy and Material Science, IITM for XRD and photocatalysis, SAIF (Sophisticated Analytical Instrument Facility) IITM for FTIR and MSRC (Material Science Research Centre) IITM for Raman, HRTEM, DRS and XPS measurements.

References

1. K.J. Sreeram, J.R. Rao, R. Sundaram, "Semi-continuous recovery of chromium from waste water", *Green Chem.*, **2** (2000) 37–41.
2. J.O. Nriagu, E. Nieboer, *Chromium in the Natural and Human Environments*, John Wiley and Sons, New York, 1988.
3. S. Luo, Y. Xiao, L. Yang, C. Liu, F. Su, Y. Li, Q. Cai, G. Zeng, "Simultaneous detoxification of hexavalent chromium and acid orange 7 by a novel Au/TiO_2 heterojunction composite nanotube arrays", *Sep. Purif. Technol.*, **79** (2011) 85–91.
4. R. Vinu, G. Madras, "Kinetics of simultaneous photocatalytic degradation of phenolic compounds and reduction of metal ions with nano-TiO_2", *Environ. Sci. Technol.*, **42** (2008) 913–919.
5. B. Sun, E.P. Reddy, P.G. Smirniotis, "Visible light Cr(VI) reduction and organic chemical oxidation by TiO_2 photocatalysis", *Environ. Sci. Technol.*, **39** (2005) 6251–6259.
6. H. Jiang, M. Li, J. Liu, X. Li, L. Tian, P. Chen, "Alkali-free synthesis of a novel heterostructured CeO_2-TiO_2 nanocomposite with high performance to reduce Cr(VI) under visible light", *Ceram. Int.*, **44** (2018) 2709–2717.
7. J. Xu, Y. Wei, Y. Huang, J. Wang, X. Zheng, Z. Sun, L. Fan, J. Wu, "Solvothermal synthesis nitrogen doped $SrTiO_3$ with high visible light photocatalytic activity", *Ceram. Int.*, **40** (2014) 10583–10591.
8. J. Müßener, P. Hille, T. Grieb, J. Schörmann, J. Teubert, E. Monroy, A. Rosenauer, M. Eickhoff, "Bias-controlled optical transitions in GaN/AlN nanowire heterostructures", *ACS Nano*, **11** (2017) 8758–8767.
9. Y.F. Zhu, D.H. Fan, G.H. Zhou, Y.B. Lin, L. Liu, "A suitable chemical conversion route to synthesize ZnO/CdS core-shell heterostructures for photovoltaic applications", *Ceram. Int.*, **40** (2014) 3353–3359.
10. Y. Lun, Y. Lin, Y. Meng, Y. Wang, "CdS quantum dots sensitized ZnO spheres via ZnS overlayer to improve efficiency for quantum dots sensitized solar cells", *Ceram. Int.*, **40** (2014) 8157–8163.
11. K. Das, S. Ghosh, K. Chakrabarti, S. Paul, G. Sinha, J. Lahtinen, D. Jana, S.K. De, "Core-shell ZnO@$CuInS_2$ hexagonal nanopyramids with improved photo-conversion efficiency", *Sol. Energy Mater. Sol. Cells.*, **143** (2015) 326–334.
12. G. Tang, S. Liu, H. Tang, D. Zhang, C. Li, X. Yang, "Template-assisted hydrothermal synthesis and photocatalytic activity of novel TiO_2 hollow nanostructures", *Ceram. Int.*, **39** (2013) 4969–4974.
13. J. Shi, C. Sun, M.B. Starr, X. Wang, "Growth of titanium dioxide nanorods in 3D-confined spaces", *Nano Lett.*, **11** (2011) 624–631.
14. D.R. Baker, P. V. Kamat, "Photosensitization of TiO_2 nanostructures with CdS quantum dots: Particulate versus tubular support architectures", *Adv. Funct. Mater.*, **19** (2009) 805–811.
15. Y. Hao, Y. Cao, B. Sun, Y. Li, Y. Zhang, D. Xu, "A novel semiconductor-sensitized solar cell based on P3HT@CdS@TiO_2 core-shell nanotube array", *Sol. Energy Mater. Sol. Cells*, **101** (2012) 107–113.
16. S. Gedi, V.R. Minnam Reddy, B. Pejjai, C. Park, C.W. Jeon, T.R.R. Kotte, "Studies on chemical bath deposited SnS_2 films for Cd-free thin film solar cells", *Ceram. Int.*, **43** (2017) 3713–3719.
17. L. Deng, H. Liu, X. Gao, X. Su, Z. Zhu, "SnS_2/TiO_2 nanocomposites with enhanced visible light-driven photoreduction of aqueous Cr(VI)", *Ceram. Int.*, **42** (2016) 3808–3815.
18. M. Wajid Shah, Y. Zhu, X. Fan, J. Zhao, Y. Li, S. Asim, C. Wang, "Facile synthesis of defective TiO_{2-x} nanocrystals with high surface area and tailoring bandgap for visible-light photocatalysis", *Sci. Rep.*, **5** (2015) 15804.
19. X. Chen, L. Liu, F. Huang, "Black titanium dioxide (TiO_2) nanomaterials", *Chem. Soc. Rev.*, **44** (2015) 1861–1885.
20. A.J. Cowan, J. Tang, W. Leng, J.R. Durrant, D.R. Klug, "Water splitting by nanocrystalline TiO_2 in a complete photoelectrochemical cell exhibits efficiencies limited by charge recombination", *J. Phys. Chem. C*, **114** (2010) 4208–4214.
21. S.K. Cushing, F. Meng, J. Zhang, B. Ding, C.K. Chen, C.J. Chen, R.S. Liu, A.D. Bristow, J. Bright, P. Zheng, N. Wu, "Effects of defects on photocatalytic activity of hydrogen-treated titanium oxide nanobelts", *ACS Catal.*, **7** (2017) 1742–1748.
22. Y.L. Li, T. Ishigaki, "Controlled one-step synthesis of nanocrystalline anatase and rutile TiO_2 powders by in-flight thermal plasma oxidation", *J. Phys. Chem. B*, **108** (2004) 15536–15542.
23. Y. Nazarkina, S. Gavrilov, H. Terryn, M. Petrova, J. Ustarroz, "Investigation of the ordering of porous anodic alumina formed by anodization of aluminum in selenic acid",

J. Electrochem. Soc., **162** (2015) E166–E172.
24. V.M. Dzhagan, M.Y. Valakh, O.E. Raevska, O.L. Stroyuk, S.Y. Kuchmiy, D.R.T. Zahn, "The influence of shell parameters on phonons in core-shell nanoparticles: A resonant Raman study", *Nanotechnology*, **20** (2009) 365704.
25. B.H. Baby, D.B. Mohan, "The formation of α-phase SnS nanorods by PVP assisted polyol synthesis: Phase stability, micro structure, thermal stability and defects induced energy band transitions", *Mater. Chem. Phys.*, **192** (2017) 317–329.
26. G. Jeantelot, S. Ould-Chikh, J. Sofack-Kreutzer, E. Abou-Hamad, D.H. Anjum, S. Lopatin, M. Harb, L. Cavallo, J.M. Basset, "Morphology control of anatase TiO_2 for well-defined surface chemistry", *Phys. Chem. Chem. Phys.*, **20** (2018) 14362–14373.
27. Y. Gao, Y. Masuda, W.S. Seo, H. Ohta, K. Koumoto, "TiO_2 nanoparticles prepared using an aqueous peroxotitanate solution", *Ceram. Int.*, **30** (2004) 1365–1368.
28. M.M. Kumar, S. Badrinarayanan, M. Sastry, "Nanocrystalline TiO_2 studied by optical, FTIR and X-ray photoelectron spectroscopy: Correlation to presence of surface states", *Thin Solid Films*, **358** (2000) 122–130.
29. U. Nithiyanantham, A. Zaki, Y. Grosu, L. González-Fernández, J.M. Igartua, A. Faik, "SiO_2@Al_2O_3 core-shell nanoparticles based molten salts nanofluids for thermal energy storage applications", *J. Energy Storage*, **26** (2019) 101033.
30. A. Sarkar, G.G. Khan, "The formation and detection techniques of oxygen vacancies in titanium oxide-based nanostructures", *Nanoscale*, **11** (2019) 3414–3444.
31. J. Ng, X. Wang, D.D. Sun, "One-pot hydrothermal synthesis of a hierarchical nanofungus like anatase TiO_2 thin film for photocatalytic oxidation of bisphenol A", *Appl. Catal. B Environ.*, **110** (2011) 260–272.
32. L. Lu, G. Wang, Z. Xiong, Z. Hu, Y. Liao, J. Wang, J. Li, "Enhanced photocatalytic activity under visible light by the synergistic effects of plasmonics and Ti^{3+} doping at the Ag/TiO_{2-x} heterojunction", *Ceram. Int.*, **46** (2020) 10667–10677.
33. Q. Yang, K. Tang, C. Wang, D. Zhang, Y. Qian, "The synthesis of SnS_2 nanoflakes from tetrabutyltin precursor", *J. Solid State Chem.*, **164** (2002) 106–109.
34. N. Stem, M.L. De Souza, D.L.A. De Faria, S.G. Dos Santos Filho, "Formation of Ti(III) and Ti(IV) states in Ti_3O_5 nano and microfibers obtained from hydrothermal annealing of C doped TiO_2 on Si", *Thin Solid Films*, **558** (2014) 67–74.
35. S.A. Ansari, M.H. Cho, "Highly visible light responsive, narrow band gap TiO_2 nanoparticles modified by elemental red phosphorus for photocatalysis and photoelectrochemical applications", *Sci. Rep.*, **6** (2016) 25405.
36. Z.H. Ibupoto, M.A. Abbasi, X. Liu, M.S. Alsalhi, M. Willander, "The synthesis of NiO/TiO_2 heterostructures and their valence band offset determination", *J. Nanomater.*, **2014** (2014) 928658.
37. T.J. Whittles, L.A. Burton, J.M. Skelton, A. Walsh, T.D. Veal, V.R. Dhanak, "Band alignments, valence bands, and core levels in the tin sulfides SnS, SnS_2, and Sn_2S_3: Experiment and theory", *Chem. Mater.*, **28** (2016) 3718–3726 .
38. Q. Wu, J. Zhao, G. Qin, C. Wang, X. Tong, S. Xue, "Photocatalytic reduction of Cr(VI) with TiO_2 film under visible light", *Appl. Catal. B Environ.*, **142-143** (2013) 142–148.
39. X. Bai, Y. Du, W. Xue, X. Hu, J. Fan, J. Li, E. Liu, "Enhancement of the photocatalytic synchronous removal of Cr(VI) and RhB over RP-modified flower-like SnS_2", *Nanoscale Adv.*, **2** (2020) 4220–4228.